Solid State Ionics 415 (2024) 116651

Contents lists available at ScienceDirect

Solid State Ionics

journal homepage: www.elsevier.com/locate/ssi

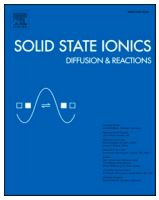

Hydride prediction during late-stage oxidation of uranium in a water vapour environment

S.R. Monisha Natchiar [a,1], Richard E. Hewitt [a,*], Phillip D.D. Monks [b]

[a] Dept. of Mathematics, University of Manchester, Manchester M13 9PL, UK
[b] AWE, Aldermaston, Berkshire RG7 4PR, UK

ARTICLE INFO

Keywords:
Reaction-diffusion
Uranium
Oxidation

ABSTRACT

We present a reaction-advection-diffusion (RAD) model for (low temperature) uranium oxidation in a water-vapour environment, where both OH^- and $H^\bullet$ are diffusing. In this model an intermediate UH_3 phase sits between the bulk U metal and a protective surface UO_2 layer. This surface oxide layer only remains adhered up to a maximum depth Δ^*_{adh} before spallation occurs leading to significantly increased diffusive transport across the spalled layer. Under these conditions, this mechanistic model is shown to support *both* a parabolic ($\propto\sqrt{t}$) oxide growth up to the point of spallation, before smoothly transitioning to a linear ($\propto t$) oxidation solution at later times. In the late-stage linear regime, a $UO_2 - UH_3$ interface propagates into the bulk metal at a constant velocity of

$$\frac{D_1^{(3)*}C^*}{2\Delta^*_{adh}N_2^*};$$

$D_1^{(3)*}$ being the diffusion coefficient of OH^- in UO_2 and C^*/N_2^* the peak relative concentration of OH^- to U. This model predicts that the intermediate hydride layer approaches a constant thickness in the linear regime, with a $UH_3 - U$ interface propagating into the bulk metal at the same velocity. The length scale of this emergent hydride layer is shown to be most sensitive to the diffusivity of OH^- in UH_3 and the corresponding reaction rate constant. Plausible parameter values are shown to lead to hydride layers < 10 nm for room temperature oxidation in a vapour pressure of 20 Torr ($\Delta^*_{adh} = 50$ nm) consistent with recent atom-probe tomography results.

1. Introduction

Uranium corrosion in water has generated considerable research interest for >60 years. Despite this focus, a consensus has yet to be achieved regarding the details of the reaction mechanism [1]. Although most present-day nuclear reactors use oxide fuels, spent nuclear fuel from first generation reactors and present-day test reactors still pose significant safety concerns. Significant quantities of uranium hydride (UH_3) found in the corrosion product of uranium metal are reported to be the cause of several pyrophoric events in some of these nuclear facilities [2]. Although oxidation of uranium in either saturated water vapour or liquid water follows the same reaction kinetics [1,3–5], here we focus on oxidation by water vapour. This study particularly finds relevance in the transient storage of nuclear fuels containing metallic uranium at room temperature and pressure conditions.

Uranium oxidises in a water vapour environment to produce uranium dioxide (UO_2) as the main corrosion product. Early work speculated on the presence of UH_3 during the corrosion process [3,6,7] suggesting the involvement of OH^- [3,7–10] as the diffusing species, while others [11–14] suggested O^{2-} as the sole diffusing species. However, a recent atom-probe tomography (APT) study by Martin et al. [9] irrefutably evidenced the presence of hydroxyl species throughout the oxide layer during water-vapour oxidation of uranium. After two hours of exposure, a 3–5 nm thick hydride layer was observed between

* Corresponding authors.
E-mail address: richard.e.hewitt@mancehster.ac.uk (R.E. Hewitt).
[1] Present address: University of Exeter, Exeter, UK.

https://doi.org/10.1016/j.ssi.2024.116651
Received 11 April 2024; Received in revised form 28 July 2024; Accepted 31 July 2024
Available online 10 August 2024

the oxide and metal layers [9]. This led the authors to conclude that UH_3 is formed as a reaction-intermediate in the oxidation of uranium in an environment containing non-saturated water vapour.

Baker et al. [3] had earlier proposed the formation of UH_3 as a reaction-intermediate, also suggesting OH^- to be the diffusing species based on hydrogen outgassing deficiencies. In this work, we consider the formation of UH_3 as a transitory reaction-intermediate during water-vapour corrosion of uranium, following the reaction scheme (2) outlined below, as first introduced by Natchiar et al. [10]. We consider intermediate (interfacial) hydride to be different from bulk hydride, the latter of which may be formed when H_2 diffuses through the porous (or cracked) oxide to react directly with the metal underneath. The formation of bulk hydride is not substantial without the accumulation of hydrogen gas (H_2) that is released during the earlier corrosion process [1] and is not investigated in this work. We restrict this study to atmospheric temperature (or low-temperature regimes <300 °C) and pressure conditions.

There is sufficient empirical evidence (see the review article [1] and references therein) to indicate a quasi-linear oxidation regime after cracking and spalling of the surface oxide. Although a few empirical models exist, to the authors' knowledge there is no predictive mechanistic model that simultaneously captures both the initial 'parabolic' (oxide thickness $\propto t^{1/2}$) and the transition to a later linear regime (oxide thickness $\propto t$). The Haycock model [15], although described as mechanistic has no explicit consideration of underpinning physicochemical processes. In this work we provide a model of the oxidation kinetics that includes the dominant physical processes of diffusion, advection and a simple spallation condition, whilst remaining tied to an explicit elementary reaction scheme.

Late-stage corrosion is considered to follow linear kinetics after cracking/spalling of the surface oxide splits it into adherent and non-adherent layers. Here, the diffusion of OH^- through the adherent oxide layer is considered to be rate-limiting. The reader is referred to [10] for a mathematical model of the early-stage uranium corrosion (before spallation), which predicts a parabolic oxide growth of thickness

$$\Delta^*_{oxide} = \left(\frac{D_1^{(3)^*} C^*}{N_3^*} t^*\right)^{1/2}; \tag{1}$$

here and elsewhere we use the asterisk notation to indicate dimensional quantities. In this expression $D_1^{(3)^*}$ is the diffusion coefficient of OH^- in UO_2; in general $D_i^{(j)^*}$ is used to denote the diffusion coefficient of diffusing species i in phase j where $j = 1, 2, 3$ enumerates UH_3, U and UO_2. C^* is the concentration of OH^- at the oxide surface, N_3^* is the concentration of UO_2 and t^* is time.

The initial square-root oxidation described by (1) can be found in previous empirical models [4,5,7] on assuming the oxide can grow without bound. In practice this oxide growth is limited and there is thought to be a recurring process of growth and breakaway the commulative effect of which is the quasi-linear oxidation regime. The thickness at which the oxide layer spalls is dependent on the development of stress/strain in the material, which is tied to complex properties of the multi-phase bulk structure and remains beyond the scope of this work. Here, we consider a simpler, constant maximum thickness of adherent oxide as a parameter in the model, assuming any growth beyond this value leads to instantaneous cracking/spalling, which allows direct access of any diffusing species to the surface of this adhered layer.

It is to be noted that the quantity of hydride formed can be substantially influenced by impurities in the metal among other factors [1,3]. Here, we do not consider the effect of metal impurities on the oxidation rate; in other words the metal is considered to be pure. Several surface-science studies [16–18] have also indicated the importance of O-defects for the dissociation of water vapour on the oxide surface. In this study, we allow for the dissociation of water vapour without explicit consideration of the crystal orientation or the stoichiometry of the surface oxide; UO_{2+x} with $x = 0 - 0.1$ is reported in water-vapour oxidation of uranium [3].

2. Reaction mechanism and assumptions

The reaction scheme described in [10] proceeds with the following elementary steps within the material

$$UH_3 + 2\ OH^- \xrightarrow{k_1^*} UO_2 + 5\ H^\bullet + 2\ e^-, \tag{2a}$$

$$U + 3\ H^\bullet \xrightarrow{k_2^*} UH_3, \tag{2b}$$

where chemical state symbols have been omitted for simplicity. A surface reaction scheme that links with the reactants and products of (2) is

$$2\ H_2O + O^{2-}_{lattice} \rightarrow 2\ OH^-_{lattice} + 2\ OH^-, \tag{3a}$$

$$2\ e^- + 2OH^-_{lattice} \rightarrow 2O^{2-}_{lattice} + H_2, \tag{3b}$$

$$2\ H^\bullet \rightarrow H_2, \tag{3c}$$

where the subscript$_{lattice}$ denotes lattice-bound species. The overall reaction is therefore

$$U\ (s) + 2\ H_2O\ (g) \rightarrow UO_2\ (s) + 2\ H_2\ (g). \tag{4}$$

Note that the oxide formed is considered to be stoichiometric [3]. The partial dissociation of water to form hydroxyl groups on the oxide surface (3a) also finds support in [7,16,19,20] (see review [1]). We assume surface conditions that enable partial dissociation of water vapour on the adherent oxide (for e.g. surface O-defects) [1,17,18].

Oxidation proceeds by diffusion of OH^- through the adherent oxide and reaction with UH_3 to form new UO_2 at the base of the adherent oxide. This releases hydrogen, some of which is outgassed through the surface layer, whilst the rest diffuses through the hydride layer to react at the $UH_3 - U$ boundary and replenish the interfacial hydride.

3. Mathematical modelling

3.1. The reaction-advection-diffusion (RAD) model

We begin from the one-dimensional RAD model [10], where the asterisk superscript is again used for dimensional quantities:

$$\frac{\partial \rho^*_{1,2}}{\partial t^*} + \frac{\partial}{\partial z^*}\left(v^* \rho^*_{1,2}\right) = \frac{\partial}{\partial z^*}\left(D^*_{1,2}\frac{\partial \rho^*_{1,2}}{\partial z^*}\right) + r^*_{1,2}, \tag{5a}$$

$$\frac{\partial \alpha^*_{1,2,3}}{\partial t^*} + \frac{\partial}{\partial z^*}\left(v^* \alpha^*_{1,2,3}\right) = R^*_{1,2,3}. \tag{5b}$$

The source/sink terms $r^*_{1,2}$ and $R^*_{1,2,3}$ arise from the reactions defined in (2) and are explicitly stated in (6) below. v^* is a spatially/temporally-varying advection velocity induced by density reductions (and therefore material expansion) during the transitions from U to UH_3 then UO_2. The concentrations being determined are both the diffusing (OH^-,$H^\bullet$) species and the bulk material volume fractions of (UH_3, U, UO_2):

$$\left(\rho^*_1, \rho^*_2\right) \equiv \left([OH^-], [H^\bullet]\right), \tag{5c}$$

$$\left(\alpha^*_1, \alpha^*_2, \alpha^*_3\right) \equiv \left([UH_3], [U], [UO_2]\right). \tag{5d}$$

The relevant diffusion coefficients are D^*_i, which denote the diffusion coefficient for ρ^*_i in the mixed phase material. Owing to the relatively low concentrations of OH^- and $H^\bullet$ present in all three phases of the material, these diffusion coefficients are only affected by the volume fractions $\alpha_{1,2,3}$, i.e., we assume the diffusion coefficients of OH^- and $H^\bullet$ do not vary with the local concentrations of these species.

For the reaction scheme specified by (2) we define

$$(r_1^*, r_2^*) = (-2k_1^*\rho_1^{*2}\alpha_1^*, 5k_1^*\rho_1^{*2}\alpha_1^* - 3k_2^*\rho_2^{*3}\alpha_2^*), \tag{6a}$$

$$(R_1^*, R_2^*, R_3^*) = (k_2^*\rho_2^{*3}\alpha_2^* - k_1^*\rho_1^{*2}\alpha_1^*, -k_2^*\rho_2^{*3}\alpha_2^*, k_1^*\rho_1^{*2}\alpha_1^*), \tag{6b}$$

where k_1^* and k_2^* are the reaction rate constants (temperature is assumed to be fixed throughout this work).

We solve the problem in a non-dimensional form. To do this we use the peak (surface) concentration of OH^- denoted by C^* and known [21] concentrations $N_{1,2,3}^*$ for pure phases of uranium hydride ($4.54{\cdot}10^{-2}$ mol cm^{-3}), uranium ($8.01{\cdot}10^{-2}$ mol cm^{-3}) and uranium dioxide ($4.06{\cdot}10^{-2}$ mol cm^{-3}) respectively:

$$\rho_{1,2}^*(z^*, t^*) = C^*\rho_{1,2}(z, t), \tag{7a}$$

$$\alpha_{1,2,3}^*(z^*, t^*) = N_{1,2,3}^*\alpha_{1,2,3}(z, t). \tag{7b}$$

We choose an arbitrary reference length scale of L_{ref}^* and the associated time scale

$$z^* = L_{ref}^* z, \quad t^* = \frac{L_{ref}^{*2}}{D_{ref}^*}\frac{N_2^*}{C^*}t, \tag{7c}$$

then a velocity scale follows directly from the ratio of length and time scales. In what follows, we choose $L_{ref}^* = 1$ nm, and $D_{ref}^* = 10^{-12}$ cm^2 s^{-1}, based on a typical value for the diffusivity of OH^- (or water-species) in UO_2 [22].

At temperatures/vapour-pressures associated with ambient room-temperature conditions, we expect the concentrations of OH^- (ρ_1^*) and $H^\bullet$ (ρ_2^*) to be substantially smaller than the bulk concentrations ($N_{1,2,3}^*$), hence $\rho_{1,2}^* \ll N_{1,2,3}^*$. It will therefore take a long time for sufficient diffusive flux to occur and move the reaction fronts into the bulk material. This long timescale is captured by (7c) above when $C^*/N_2^* \ll 1$. In this regime the non-dimensional RAD model simplifies to one of quasi-steady diffusion:

$$\frac{\partial}{\partial z}\left(D_{1,2}\frac{\partial \rho_{1,2}}{\partial z}\right) = r_{1,2}, \tag{8a}$$

$$\frac{\partial \alpha_{1,2,3}}{\partial t} + \frac{\partial}{\partial z}(v\alpha_{1,2,3}) = R_{1,2,3}, \tag{8b}$$

where

$$(r_1, r_2) = (2k_1\rho_1^2\alpha_1, 3k_2\rho_2^3\alpha_2 - 5k_1\rho_1^2\alpha_1), \tag{8c}$$

$$(R_1, R_2, R_3) = \left(\left(k_2\rho_2^3\alpha_2 - k_1\rho_1^2\alpha_1\right)\frac{N_2^*}{N_1^*}, -k_2\rho_2^3\alpha_2, k_1\rho_1^2\alpha_1\frac{N_2^*}{N_3^*}\right), \tag{8d}$$

and the dimensionless reaction coefficients are

$$k_1 = \frac{k_1^* C^* N_1^* L_{ref}^{*2}}{D_{ref}^*}, \quad k_2 = \frac{k_2^* C^{*2} N_2^* L_{ref}^{*2}}{D_{ref}^*}. \tag{8e}$$

These are essentially Damköhler numbers for each reaction, based on the reference length scale and diffusivity.

A simple volume-fraction weighted combination of the diffusivity coefficients is employed,

$$D_{1,2} = \sum_{j=1,2,3} D_{1,2}^{(j)}\alpha_j, \tag{8f}$$

where $D_{1,2}^{(j)}$ is the constant diffusivity of OH^- and $H^\bullet$ in a region where $\alpha_j = 1$. For $t \geq 0$ the boundary conditions are a fixed surface concentration of OH^-

$$\rho_1 = 1, \quad \rho_2 = 0 \quad \text{at} \quad z = z_s(t), \tag{8g}$$

with an unreacted metal far away from the surface,

$$\rho_1, \rho_2 \to 0, \quad (\alpha_1, \alpha_2, \alpha_3) \to (0, 1, 0) \quad \text{as} \quad z \to -\infty. \tag{8h}$$

This model was derived for the parabolic oxidation regime, where the surface oxide layer remains intact throughout exposure. However in the linear oxidation regime there is breakup of the surface oxide layer and the domain is shown in Fig. 1. The difference lies with the upper cracked/porous oxide layer, and underlying adherent oxide which has a maximum depth (Δ_{adh}^*). We will discuss an approach to modelling this configuration within the confines of (8) in Section 4.2.

3.2. Typical parameter values

Solution of the RAD model above requires values for six diffusivity coefficients ($D_i^{(j)*}$), corresponding to the two diffusing entities in three phases, two reaction rates ($k_{1,2}^*$) in (2), the maximum adherent layer thickness (Δ_{adh}^*) and the peak concentration (C^*) of OH^-. In the discussion below, we restrict ourselves to room temperature conditions. As a reminder, the subscript i in $D_i^{(j)*}$ denotes the diffusing species and the superscript (j) denotes the phase (i.e. $j = 1, 2, 3$ correspond to phases UH_3, U and UO_2 respectively).

We will start from a reference set for these values, as presented in Table 1, some of which can be approximated from existing work, while others are necessarily ad hoc choices. Later results (and Table 2) introduce distributions for all the parameters listed in Table 1, enabling us to characterise the sensitivity of predictions for the internal hydride layer to these reaction and diffusion parameters.

The distribution describing $D_2^{(1)*}$ follows from linear regression of the data presented in Fig. 4 of Peretz et al. [23], which provides an estimate of the mean and standard deviation for the activation energy of the hydrogen jump frequency in β-UH_3. Using random sampling to combine the resulting quantities with the reported uncertainty in the Arrhenius pre-exponential, and using the UH_3 lattice parameter to convert jump frequency to diffusion coefficient, results in the distribution in the room temperature value provided in Table 2.

The distribution describing $D_2^{(2)*}$ is obtained from Arrhenius analysis

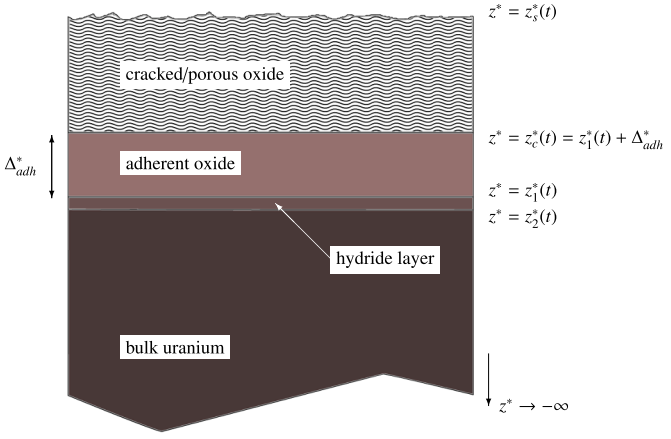

Fig. 1. A schematic diagram of the late-stage oxidation, where a cracked/porous upper layer has developed. As the layers move into the bulk uranium a recurring cracking/spalling of the oxide is approximated as a constant thickness (Δ_{adh}^*) adhered oxide layer. Although the oxide/hydride/bulk regions are shown as distinct regions, there is a rapid (smooth) transition between each, associated with two propagating reaction fronts at $z^* = z_{1,2}^*$.

Table 1
Representative choices for the dimensional parameters associated with diffusivity and reaction rates.

$D_1^{(j)*};\ j=1,2,3$	$D_2^{(1)*}$	$D_2^{(2)*}$	$D_2^{(3)*}$	k_1^*	k_2^*
$cm^2\ s^{-1}$	$cm^2\ s^{-1}$	$cm^2\ s^{-1}$	$cm^2\ s^{-1}$	$mol^{-2}\ cm^6\ s^{-1}$	$mol^{-3}\ cm^9\ s^{-1}$
$10^{-12}\left(=D_{ref}^*\right)$	$8.94{\cdot}10^{-16}$	$1.49{\cdot}10^{-10}$	$1.18{\cdot}10^{-13}$	10^8	10^{15}

Table 2
Log-normal distributions of values for the diffusivity of (top to bottom) $H^\bullet$ in UH_3, U and UO_2 at a temperature of 25 °C. Here the values are obtained from Peretz et al. [23] for $D_2^{(1)*}$, Mallett and Trzeciak [24] for $D_2^{(2)*}$ and Wheeler [25], for $D_2^{(3)*}$.

Diff. coeff. ($cm^2\ s^{-1}$)	mean	mean (log)	SD (log)
$D_2^{(1)*}$	$8.94{\cdot}10^{-16}$	− 34.65	1.06
$D_2^{(2)*}$	$1.49{\cdot}10^{-10}$	− 22.63	0.41
$D_2^{(3)*}$	$1.18{\cdot}10^{-12}$	− 27.46	1.16

of the temperature-dependent diffusion coefficient data for hydrogen in α-U presented in table 4 of Mallett and Trzeciak [24]. Data are extrapolated to 298.15 K, where the standard deviation is estimated from the 95% confidence interval for the predicted mean value. Likewise, the distribution for $D_2^{(3)*}$ results from the same methodology applied to the temperature-dependent diffusion coefficient data for hydrogen in UO_2 single crystals presented in Fig. 4 of Wheeler [25].

For diffusion of OH^- in the three bulk phases (i.e. $D_1^{(j)*}$) we take all three values to be equal to the reference diffusivity ($10^{-12}\ cm^2\ s^{-1}$), which is chosen as a typical value for the diffusivity of OH^- (or water-species) in UO_2 [22].

For the maximum adherent layer thickness we appeal to Table 2 from [26] (albeit for oxidation in pure O_2 environments) and the results of [1] in water/water-vapour. The thickness of the adherent layer varies for different ambient environments and typically thickens at higher temperatures; herein we restrict attention to a representative room-temperature value of 50 nm.

For the reaction rates in (2) we choose ad hoc reference values of $k_1^* = 10^8\ mol^{-2}\ cm^6\ s^{-1}$ and $k_2^* = 10^{15}\ mol^{-3}\ cm^9\ s^{-1}$.

Finally for C^* (the peak concentration of OH^-), we shall first derive (see Section 4) a simple theoretical relationship for the linear-regime oxidation rate, then use this to infer a value of C^* consistent with available empirical data. The review paper of Banos and Scott [27] provides the following empirical fit for the (linear regime) oxidation rate of U (denoted as k^* in their work) in a water-vapour environment with water-vapour pressure $P_{H_2O}^*$ for the low-temperature regime (< 300 °C) and vapour-pressure ≤ 1013.25 mbar:

$$k^* = 1.6114{\cdot}10^5 \left(P_{H_2O}^*\right)^{\frac{1}{2}} exp\left(-\frac{5396.8\mathrm{K}}{T^*}\right) \mathrm{mgU\,cm^{-2}\,h^{-1}}, \tag{9}$$

where $P_{H_2O}^*$ is measured in millibars. This expression is eq. (6) from [27]:

$$lnK^* = 11.99 - \left(\frac{5396.8}{T^*}\right), \tag{10}$$

where $K^* = k^*/\left(P_{H_2O}^*\right)^{0.5}$.

With a density for U of 19.06 $g\ cm^{-3}$, this reduces to

$$8.4544{\cdot}10^7 \left(P_{H_2O}^*\right)^{\frac{1}{2}} exp\left(-\frac{5396.8\,\mathrm{K}}{T^*}\right) \mathrm{nm\ h^{-1}}. \tag{11}$$

Evaluated at a temperature of 25 °C and a vapour pressure of 20 Torr (26.66 mbar) the material is corroded at a rate of approximately 6 $nm\ h^{-1}$ with a loss of U of approximately $1.14{\cdot}10^{-2}\ mg\ cm^{-2}\ h^{-1}$.

4. A constant-rate oxidation solution

An extensive analysis of (8) is given by Natchiar et al. [10], providing both computational results and a theoretical description (valid at large exposure times) under the assumption that the adhered oxide layer can grow without bound. Following some initial transient behaviour associated with the details of the initial state of the material, it was shown that the thickness of this adherent layer ultimately grows parabolically ($\propto t^{1/2}$) and that the oxide remains separated from the bulk uranium by a UH_3 layer.

In the RAD model (8), the generic theoretical behaviour is that the intermediate hydride layer also thickens like $\delta t^{1/2}$ (for some constant δ) in tandem with the oxide layer. However a notable feature is that the diffusivity of $H^\bullet$ in UH_3 is small compared to that of OH^- in UO_2 (i.e., $D_2^{(1)*}/D_1^{(3)*} \ll 1$ as in Table 1). It has been shown that this limit is a special case for the RAD model; the thickness of the UH_3 layer becomes proportional to $t^{1/4}k_1^{-1/4}$ (in the notation of Natchiar et al., as shown in Fig. 7 of that work). Of course these predictions are based on the assumption of a sufficiently long exposure of the material, while still neglecting the break up of any surface oxide layer.

As the oxide layer grows, diffusive flux of OH^- to the reaction front is reduced, and it is this fundamental mechanism that leads to an eventual parabolic behaviour for early-stage oxidation. However, the assumption of an adherent oxide layer that grows without limit is obviously expected to fail at some point. The oxide layer is known to crack and spall (Fig. 1), the effect of which is to provide an upper limit for the (adhered) oxide thickness (Δ_{adh}^*). In this model we will take this upper limiting thickness to be a constant rather than imposing any recurring growth/spall process. Beyond this limit, the flux of OH^- stops decreasing and this motivates the examination of constant-flux solutions to the same RAD model provided by (8). Determining the size of the adherent layer (i.e., Δ_{adh}^*) from first principles is beyond the scope of this model, as it must depend upon the mechanical properties of the oxide and any stress distribution within the material; instead we seek a solution where the maximum adherent layer thickness is imposed as a parameter.

In the late-stage linear regime, we suppose that the top of the adhered oxide layer (see Fig. 1) is given by $z_c = z_c^*/L_{ref}^* = \xi_c - Vt$, where V is the (dimensionless) propagation velocity and ξ_c an offset. The value ξ_c is determined by the full history of the evolution and remains arbitrary when considering only the late-stage linear behaviour, so we take $\xi_c = 0$ here without loss of generality. We now seek a *uniformly* translating solution to (8) via a ξ coordinate defined by

$$z = \xi - Vt, \tag{12}$$

where V is a constant to be found, which determines the rate of the shrinking core' during oxidation. The domain of solution is now $\xi \in (-\infty, 0]$, with two (now stationary in the ξ frame) reaction fronts at $\xi = \xi_{1,2}$ where the two reactions of (2) dominate. Here $\xi_{1,2}$ correspond to the points indicated in the dimensional schematic of Fig. 1 as $z_{1,2}^*$.

In the translating coordinate, assuming an otherwise steady solution results in the ordinary-differential system

$$\frac{\mathrm{d}}{\mathrm{d}\xi}\left(D_{1,2}\frac{\mathrm{d}\rho_{1,2}}{\mathrm{d}\xi}\right) = r_{1,2}, \tag{13a}$$

$$V\frac{\mathrm{d}\alpha_{1,2,3}}{\mathrm{d}\xi}+\frac{\mathrm{d}}{\mathrm{d}\xi}\left(v\alpha_{1,2,3}\right)=R_{1,2,3}, \tag{13b}$$

where $D_{1,2}$ remain dependent on ξ through (8f).

A cracked/porous oxide allows direct access of water vapour to the top surface of the adhered oxide layer, leading to the boundary conditions

$$\rho_1=1,\quad \rho_2=0\quad \text{at}\quad \xi=0, \tag{13c}$$

$$\rho_1,\rho_2\to 0,\quad (\alpha_1,\alpha_2,\alpha_3)\to(0,1,0)\quad \text{as}\quad \xi\to-\infty. \tag{13d}$$

This final condition requires that we recover unreacted U sufficiently deep into the metal.

While solution of (13) will provide the local behaviour, we can predict the bulk behaviour by integration from $\xi=-\infty$ to $\xi=0$ (assuming that the surface layer reduces to a pure oxide phase). This results in

$$D_1^{(3)}\frac{\mathrm{d}\rho_1}{\mathrm{d}\xi}\bigg|_{\xi=0}=2I_1,\quad D_2^{(3)}\frac{\mathrm{d}\rho_2}{\mathrm{d}\xi}\bigg|_{\xi=0}=3I_2-5I_1, \tag{14a}$$

$$I_2=I_1,\quad V=I_2,\quad V+v_c=I_1N_2^*/N_3^*, \tag{14b}$$

where $v_c=v(\xi=0)$ is the advection velocity of the surface of the adherent oxide layer (as induced by material expansion during the reaction process). The two quantities $I_{1,2}$ are related to the total consumption/production of OH^- and $H^\bullet$ via:

$$I_1=k_1\int_{-\infty}^{0}\rho_1^2\alpha_1\,\mathrm{d}\xi,\quad \text{and}\quad I_2=k_2\int_{-\infty}^{0}\rho_2^3\alpha_2\,\mathrm{d}\xi. \tag{14c}$$

Eliminating $I_{1,2}$ in (14a) leads us to conclude

$$V=\frac{D_1^{(3)}}{2}\frac{\mathrm{d}\rho_1}{\mathrm{d}\xi}\bigg|_{\xi=0},\quad v_c=V\left(N_2^*/N_3^*-1\right). \tag{15}$$

Diffusion of OH^- in the adherent oxide layer is quasi-steady. Hence a good approximation (as confirmed in Fig. 2 discussed below) for ρ_1 in the adherent layer is a simple constant flux state:

$$\rho_1\approx 1+\frac{\xi}{\Delta_{adh}}. \tag{16}$$

This satisfies $\rho_1(0)=1$ and $\rho_1(-\Delta_{adh})=0$, where the latter state is associated with a reaction front at $\xi=\xi_1=-\Delta_{adh}$ at which all the OH^- is consumed. Therefore

$$V=\frac{1}{2}\frac{D_1^{(3)}}{\Delta_{adh}}. \tag{17}$$

Hence, in this regime, the reaction fronts, adherent oxide and hydride layers all propagate into the bulk metal with a constant dimensional velocity of

$$V^*=\frac{D_1^{(3)*}}{2\Delta_{adh}^*}\frac{C^*}{N_2^*}. \tag{18}$$

Here $\Delta_{adh}^*=L_{ref}^*\Delta_{adh}$ is a dimensional thickness of the adherent layer, $D_1^{(3)*}$ is the diffusion coefficient for OH^- in UO_2, C^* is the near-surface concentration of OH^- and N_2^* is the number density of U.

For consistency between this constant oxidation rate solution to (8) and the empirical observation (11) we require (for example, at 25 °C and a vapour pressure of 20 Torr) that $V^*=6.07$ nm h^{-1}. So for any given

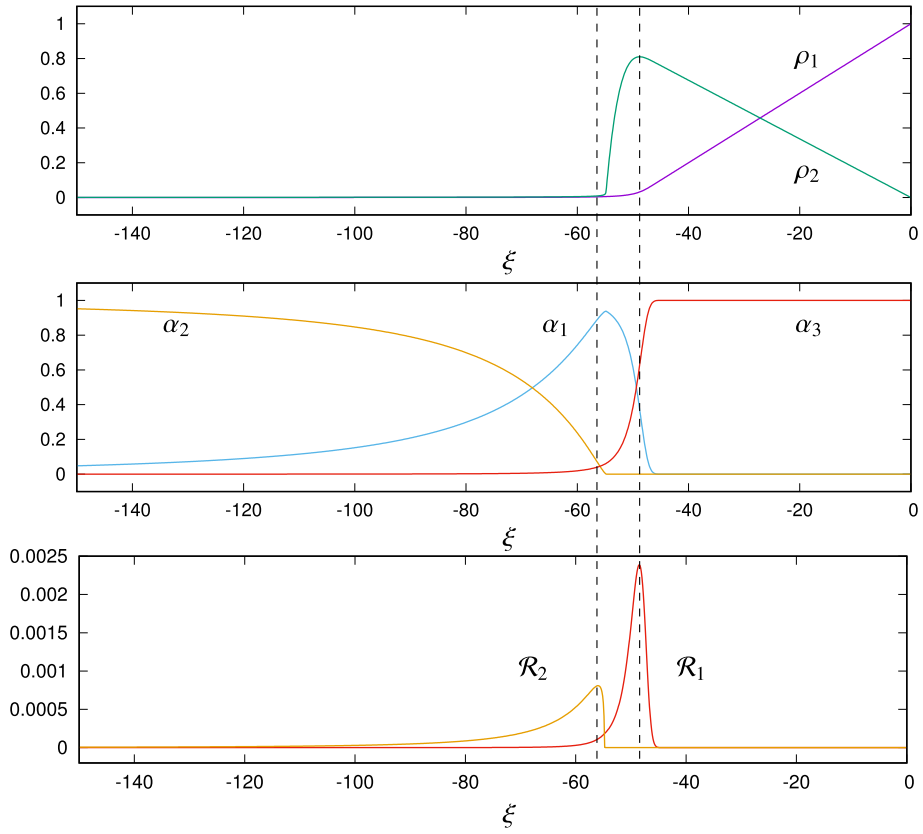

Fig. 2. An example solution of the steady problem (13), for a uniformly translating reaction front state associated with the linear oxidation regime. Here the (dimensionless) adhered oxide depth is 50. Dimensionless parameters are $D_2^{(1)}=8.94{\cdot}10^{-4}$ (a measure of the diffusion coefficient of $H^\bullet$ in UH_3), $D_2^{(2)}=149$ ($H^\bullet$ in U), $D_2^{(3)}=1.18$ ($H^\bullet$ in UO_2) consistent with Table 1, $D_1^{(i)}=1$ (the diffusion coefficient of OH^- in all three phases is the reference value) and $k_1=6.13$, $k_2=14611$ are the relative reaction rates (8e). The two (vertical) dashed lines indicate the reaction front positions $\xi=\xi_{1,2}$, which maximise reaction rates $\mathcal{R}_{1,2}$ defined by (20).

values of $D_1^{(3)*}$ and Δ^*_{adh}, we can obtain a value for C^* from (18) that will give results consistent with observation. The default values of Table 1 with $\Delta^*_{adh} = 50$nm leads to $C^* = 1.3510^{-4}$ mol cm^{-3}.

The expression (18) can be obtained more directly by considering the surface flux of oxygen required to produce UO_2 at the correct empirical rate (11), without recourse to any detailed RAD model. A more interesting (and a much more sensitive metric to assess the model) is the corresponding prediction for the hydride layer thickness, which we will obtain from numerical solution of (13).

From (14a) we can confirm that the hydride layer should be of constant thickness (in the linear regime), by noting that the flux of OH^- into the bulk is balanced by the outward flux of $H^\bullet$:

$$D_1^{(3)}\frac{d\rho_1}{d\xi}\bigg|_{\xi=0} + D_2^{(3)}\frac{d\rho_2}{d\xi}\bigg|_{\xi=0} = 0. \tag{19}$$

So the growth of the interfacial hydride layer happens during the initial transient/parabolic stage, and once in the linear oxidation phase its volume remains constant.

4.1. Numerical solutions of the constant-rate oxidation regime

The constant-rate oxidation system (13) can be computed by standard methods. At fixed values of the dimensionless parameters $k_{1,2}$ and $D_i^{(j)}$ we can obtain solutions that correspond to a dimensionless adherent layer thickness of Δ_{adh}, by taking $V = D_1^{(3)}/(2\Delta_{adh})$ as given by (17).

Fig. 2 presents the solution obtained for $\Delta_{adh} = 50$ (with other parameter values taken to be the reference values discussed in Section 3.2). The figure shows $\rho_{1,2}$, volume fractions $\alpha_{1,2,3}$ and the two reaction terms

$$\mathcal{R}_1(\xi) = k_1\rho_1^2\alpha_1, \quad \mathcal{R}_2(\xi) = k_2\rho_2^3\alpha_2. \tag{20}$$

Unlike the parabolic response at earlier times, in the linear oxidation regime described here a key feature is that these reaction fronts maintain a *constant* separation in line with (19). A natural thickness measure for the UH_3 layer is therefore

$$\Delta^*_{UH_3} = L^*_{ref}(\xi_1 - \xi_2), \tag{21}$$

where the asterisk again signifies a dimensional quantity and $\xi_{1,2}$ are the locations of the respective maxima of $\mathcal{R}_{1,2}$.

Fig. 2 also demonstrates that the return to an unreacted U state (i.e. $\alpha_2 = 1$) can occur relatively slowly depending on the precise parameter values chosen. As an additional measure we therefore also consider the total mass of UH_3 (per unit area of material), as obtained from depth integration of the volume fraction:

$$I^*_{UH_3} = L^*_{ref}M^*_1\int_{-\infty}^{0}\alpha_1(\xi)\,d\xi, \tag{22}$$

where M^*_1 is the (mass) density of UH_3 (approximately 10.95 g cm^{-3}).

Numerical solutions of (13) indicate that $\Delta^*_{UH_3}$ is most sensitive to $D_1^{(1)}$ (relative diffusivity of OH^- in UH_3) then k_1 (the dimensionless reaction rate constant for UH_3 and OH^-). This is consistent with the asymptotic behaviour described by Natchiar et al. [10], where again $D_1^{(1)}$ and the first reaction rate dominated the hydride thickness for large times in the parabolic regime (in cases of $D_2^{(1)} \ll 1$, as is the case here).

An examination of $I^*_{UH_3}$ shows that it is most sensitive to the values of $D_2^{(2)}$ (relative diffusivity of $H^\bullet$ in U) and k_2 (the dimensionless reaction rate constant for U and $H^\bullet$). For smaller relative diffusivity coefficients or faster reaction rates, the return to unreacted U within the metal occurs over a smaller length scale (as expected).

In Figs. 3(a,b) we show the dependence of $\Delta^*_{UH_3}$ and $I^*_{UH_3}$ as functions of the two relevant dominant parameters (being $D_1^{(1)}$, k_1 and $D_2^{(2)}$, k_2 respectively). We return to these predictions below to compare full (unsteady) solutions to the RAD model with randomised parameter choices.

4.2. Evolution through to late-stage oxidation

To validate the conclusions drawn from (13) discussed above, we return to the original initial-value problem posed by (8) and time march

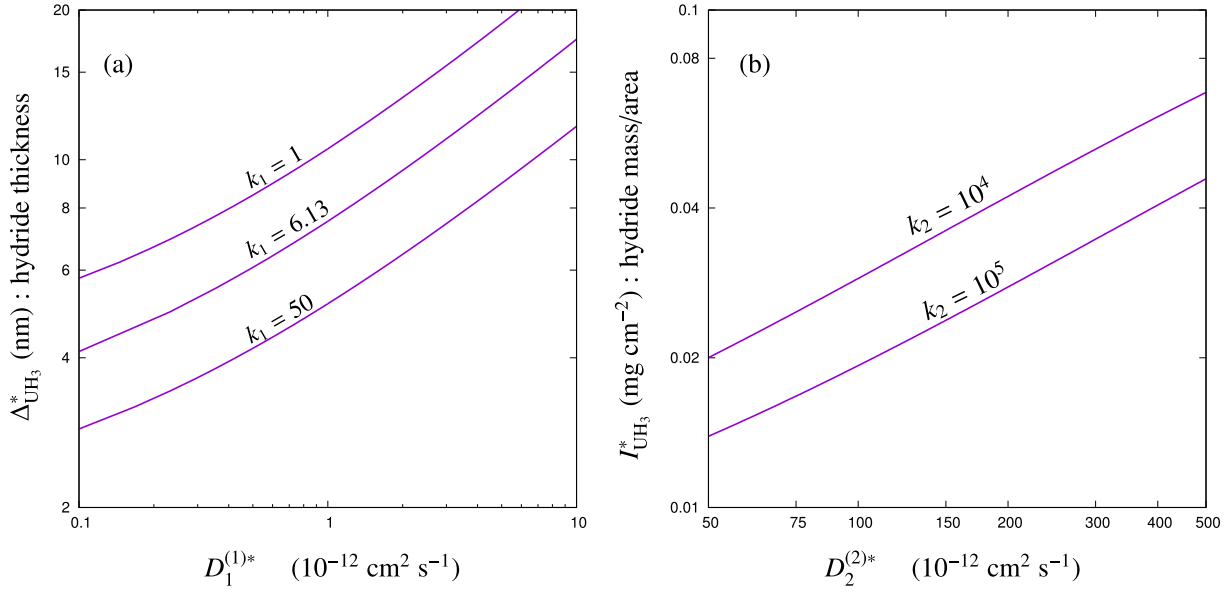

Fig. 3. Solutions of (13) with a dimensionless advection velocity $V = D_1^{(3)}/(2\Delta_{adh})$ and $\Delta_{adh} = 50$ (i.e., a 50 nm adherent layer): (a) thickness of the hydride layer defined by the reaction front positions via (21), $k_1 \in [1, 50]$ corresponds to dimensional reaction rates in the reaction scheme (2) in the range $k_1^* \in [1.6{\cdot}10^7, 8.2{\cdot}10^8]$ mol^{-2}cm^{6}s^{-1} and $D_1^{(1)*}$ is the diffusion coefficient of OH^- in UH_3, (b) mass (per unit area) of hydride defined by the integrated measure (22), $k_2 \in [10^4, 10^5]$ corresponds to dimensional reaction rates in the reaction scheme (2) in the range $k_2^* \in [6.8{\cdot}10^{14}, 6.8{\cdot}10^{15}]$ mol^{-3}cm^{9}s^{-1} and $D_2^{(2)*}$ is the diffusion coefficient of $H^\bullet$ in U. Any parameters not shown are fixed at the values specified in Table 1.

the system, following the same procedure outlined by Natchiar et al. [10]. For a simplistic model of the cracked/porous oxide (as shown in Fig. 1) the diffusivity of OH^- and $H^\bullet$ is increased by three orders of magnitude in the region $z > z_c(t) = z_1(t) + \Delta_{adh}$ where Δ_{adh} is a specified constant. This large increase in diffusion through the non-adherent oxide leads to an approximately constant concentration of OH^- in the cracked/porous region.

For early times, where the oxide thickness is less than Δ^*_{adh} the problem is that described by Natchiar et al., but beyond the point of breakaway, which is achieved when $z_s(t) > z_c(t)$, we expect to transition to a constant flux (of OH^-), revealing the constant-rate oxidation state discussed in Section 4.

As the system evolves, we will focus on analogous metrics for (now unsteady) hydride production (i.e., $\Delta^*_{UH_3}$ and $I^*_{UH_3}$), together with additional measures for the mass loss/gain of each phase

$$I^*_{UH_3} = L^*_{ref} M^*_1 \int_{-\infty}^{0} \alpha_1(z,t)\,\mathrm{d}z, \tag{23a}$$

$$I^*_{U} = L^*_{ref} M^*_2 \int_{0}^{-\infty} (1-\alpha_2(z,t))\,\mathrm{d}z, \tag{23b}$$

$$I^*_{UO_2} = L^*_{ref} M^*_3 \int_{-\infty}^{0} \alpha_3(z,t)\,\mathrm{d}z, \tag{23c}$$

where $M^*_1 = 10.95\ \mathrm{g\ cm^{-3}}$, $M^*_2 = 19.06\ \mathrm{g\ cm^{-3}}$ and $M^*_3 = 10.97\ \mathrm{g\ cm^{-3}}$ are the (mass) densities for UH_3, U and UO_2 respectively. Here $I^*_U < 0$ is the mass loss of U while $I^*_{UO_2} > 0$ is the mass gain of UO_2 (per unit area) and the definition of $I^*_{UH_3}$ is consistent with that presented earlier (22) but using the non-translating coordinate.

We consider 150 evolutions (for an adherent oxide thickness of 50 nm) with a water vapour pressure of 20 Torr at room temperature. In each evolution the seven dimensionless parameters in (8) are randomised, with $D^{(j)}_2$ chosen according to the log-normal distributions described by Table 2 while other parameters are chosen to cover two orders of magnitude with

$$D^{(j)*}_1 \in \left[10^{-13}, 10^{-11}\right]\ \mathrm{cm^2\,s^{-1}}, \tag{24a}$$

$$k^*_1 \in \left[10^{7}, 10^{9}\right]\ \mathrm{mol^{-2}\,cm^6\,s^{-1}} \quad \text{and} \quad k^*_2 \in \left[10^{14}, 10^{16}\right]\ \mathrm{mol^{-3}\,cm^9\,s^{-1}}, \tag{24b}$$

where the exponent is chosen from a uniform distribution.

Fig. 4(a) shows the measures (23) over a 10 h exposure for the 150 randomised evolutions. A parabolic phase is apparent in the first few hours with $\sqrt{t^*}$ growth of $I^*_{UO_2}$, until the oxide has grown sufficiently to reach the Δ^*_{adh} limit of 50 nm. Beyond this point there is a smooth transition towards a linear response for sufficiently long exposure times, and the constant-rate oxidation solution of Section 4 becomes apparent. The mass of hydride produced is consistent with the prediction arising from (13) as shown by the dashed line (B) in Fig. 4(a), which is obtained using only the reference values of Table 1. Similarly, within the first few hours the (asymptotic) prediction of oxide mass obtained from Natchiar et al. [10] works well, using eq. (6.1) in that work.

Fig. 4(b) compares the percentage of (total) outgassed hydrogen (as the reaction proceeds) with the prediction of the overall reaction (4) over a 24 h period. Initially the model predicts a growing deficit as hydrogen produced in the reaction that forms UO_2 is captured by the growth of the intermediate hydride layer. However once spallation begins and the system enters the linear regime, the hydride layer stops growing. In this linear regime the hydride enters a steady-state balance where any new hydrogen captured at the metal-hydride reaction site is released at the oxide-hydride reaction site as the U core shrinks. So whilst the hydride layer retains some hydrogen, this ratio begins to reduce compared to the increasing quantity of hydrogen being released in the linearly shrinking core. The large time behaviour is therefore a (relatively slow) recovery towards the expected (total) hydrogen production once the corrosion depth is large compared to the hydride

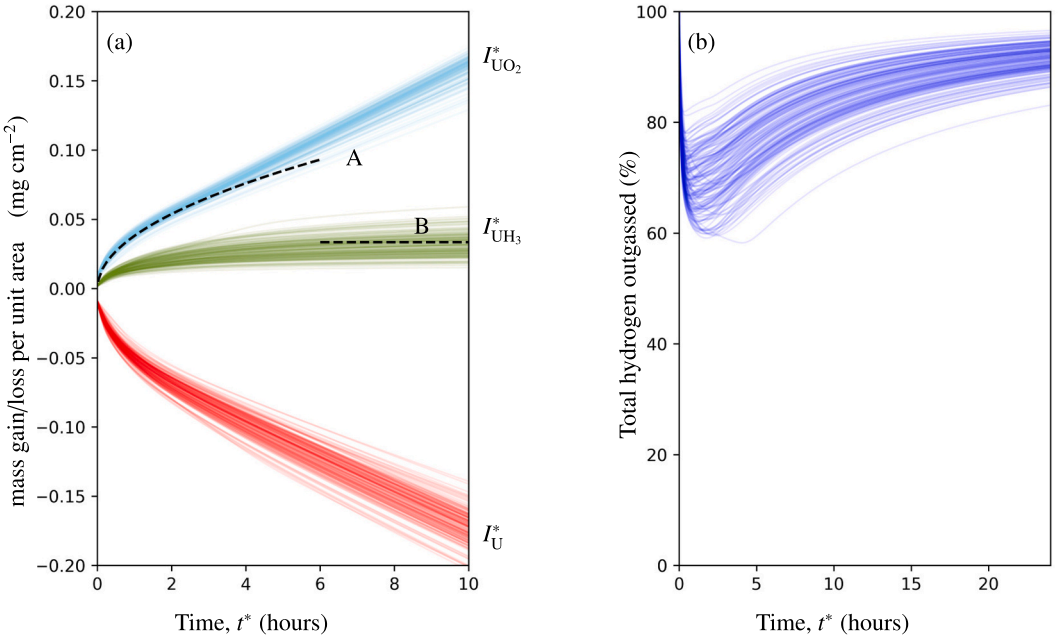

Fig. 4. An ensemble of 150 evolutions to the initial-value problem (8), spanning the parameter range listed in Table 2 and (24) with an adherent layer of thickness $\Delta^*_{adh} = 50$ nm. (a) Measures of the mass gain/loss of each phase are shown ($I^*_{UO_2}$ blue, $I^*_{UH_3}$ green and, I^*_U red) as defined by (23). Dashed lines indicate (A) the prediction of Natchiar et al. [10] for oxide growth in the parabolic stage, (B) the prediction for hydride production from the solution of Section 4. (b) The percentage of total hydrogen outgassed as the reaction proceeds compared with the theoretical prediction of the overall reaction (4), showing a time-dependent hydrogen deficit. (For interpretation of the references to colour in this figure legend, the reader is referred to the web version of this article.)

thickness.

We can also compare the mass of hydride once the evolution is well into the linear regime (i.e., after 24 h of exposure) with the predictions obtained from (13). The predictions of Fig. 3 are obtained by varying only the two dominant parameters shown in each sub-figure, while keeping all others at the reference values of Table 1. In this section all parameters are randomised according to Table 2 and (24), so we can compare both approaches as shown in Fig. 5.

Fig. 5(a) shows the thickness of the hydride region (as measured by the spatial separation of the two peaks in reaction rates $k_1\rho_1^2\alpha_1$ and $k_2\rho_2^3\alpha_2$). The two red lines in the figure repeat the ($k_1 = 1, 50$) data of Fig. 3(a). The two parameters of $D_1^{(1)^*}$ (diffusion coefficient of OH^- in UH_3) and k_1^* (the reaction rate constant for OH^- and UH_3 appearing in (2)) capture the variation of hydride thickness.

Fig. 5(b) shows the total (depth integrated) mass of hydride. Again the two red lines are the predictions of 3(b) at two fixed values of the second reaction rate constant k_2^* (or its dimensionless analogue k_2). For this metric the two parameters $D_2^{(2)^*}$ (diffusion coefficient for $H^\bullet$ in U) and k_2^* (the reaction rate constant for $H^\bullet$ and U) capture the bulk of variability.

5. Conclusions

The RAD model (8) was presented as a mechanistic model for uranium oxidation in a water-vapour environment, but only investigated in detail in the early (parabolic) regime prior to cracking/spalling of the evolving surface oxide layer [10]. Of more practical interest is the later (linear) regime, where empirical evidence indicates a transition to oxidation at a constant rate for sufficiently long exposure times. In this work we have extended the same RAD model to a constant surface flux of OH^- consistent with a late-stage cracked/porous oxide layer, by assuming a greatly enhanced diffusion beyond an adherent layer of some fixed thickness Δ_{adh}^*. This modified model then captures both the parabolic and linear oxidation regimes and allows a prediction of the quantities of interfacial hydride produced.

Hydride production is characterised by two measures (i) $\Delta_{UH_3}^*$ the spatial separation between the two reaction fronts of (2) where hydride is produced/consumed and (ii) $I_{UH_3}^*$ a depth integrated mass (of UH_3) per unit area. When in the linear oxidation regime the first measure is dominated by the diffusivity of OH^- in UH_3 ($D_1^{(1)^*}$) and the first reaction rate constant as confirmed by Fig. 5(a). The second measure is dominated by the diffusivity coefficient of $H^\bullet$ in UH_3 ($D_2^{(2)^*}$) and the second reaction rate constant, as confirmed by Fig. 5(b).

Evidence from the atom probe tomography (APT) experiments of Martin et al. [9] points to a hydride region of approximately 5 nm thick after an hour of exposure in ambient conditions, so this should be considered a lower bound to the equilibrated layer size ($\Delta_{UH_3}^*$) in the linear oxidation regime. Fig. 4 demonstrates that there are plausible choices of diffusivity coefficients and reaction rates that lead to comparable length scales. The second metric $I_{UH_3}^*$ is bounded below by $M_1^*\Delta_{UH_3}^*$ (approximately the mass associated with the hydride region per unit area) but above this it becomes a measure of the length scale over which the transition from UH_3 to U occurs. For example, Fig. 2 shows a relatively slow recovery of α_2 from 0 to 1 over a length scale of about 50 nm (for $L_{ref}^* = 1$ nm), this is too slow to be consistent with the concentration profiles recovered from the APT experiments. Fig. 6(a) from Martin et al. suggests that the recovery to a region of unreacted metal occurs over a span of closer to 10 nm, so any experimental refinement of the values for k_2^* and $D_2^{(2)^*}$ would have to lead to values for $I_{UH_3}^*$ at the lower end of the range shown in Fig. 5(b) for this RAD model to be consistent with observations.

Whilst this model is able to reproduce the initial parabolic oxide growth, transition to linear growth and an associated intermediate hydride layer that remains thin, there are features reported in the literature that still remain unexplained. The early experimental work of Baker et al. [3] indicated a hydrogen production deficit of 1–13% (p2517) when compared with the theoretical prediction of the overall reaction (4). Of course a deficit is also predicted by our model (Fig. 4b), consistent with hydrogen being 'lost' to the intermediate hydride layer. However, Baker et al. also claim that the hydrogen deficit "remains unaltered during corrosion (table 3)". The model we propose here cannot support such constant-deficit behaviour for large exposure times because the oxide layer is growing linearly with time (albeit with spallation), whilst the amount of hydride remains constant, leading to a slow decay of any deficit in total hydrogen outgassed. The only way the deficit can remain unaltered during corrosion is if the hydride layer grows linearly in time to match the oxide production. Such a scenario cannot exist because the linear oxidation regime is associated with a constant flux of OH^-, this in turn produces a constant flux of $H^\bullet$ into the UH_3 layer, which is insufficient to support a linearly thickening hydride layer.

This apparent discrepancy may be resolved by consideration of the

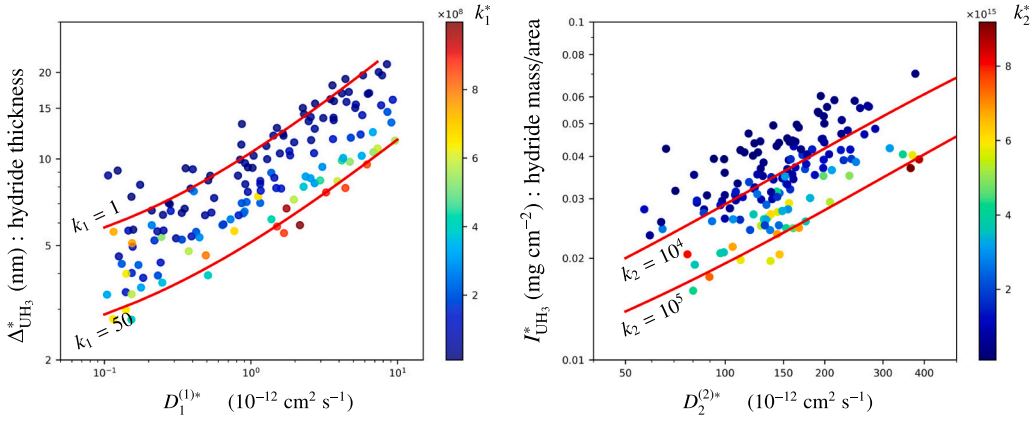

Fig. 5. Equilibrated (a) hydride thickness and (b) mass of hydride (per sq. cm of material) after 24 h of exposure, at room temperature and 20 Torr water vapour pressure, assuming a 50 nm adherent layer. Data are extracted from the randomised evolutions of Fig. 4 and colours indicate the corresponding values of the dimensional reaction rates k_1^* $\left(\text{mol}^{-2}\ \text{cm}^6\ \text{s}^{-1}\right)$ and k_2^* $\left(\text{mol}^{-3}\ \text{cm}^9\ \text{s}^{-1}\right)$. The solid red lines are the prediction obtained from (13) as presented in Fig. 3. $D_1^{(1)^*}$ is the diffusion coefficient of OH^- in UH_3 and $D_2^{(2)^*}$ is the diffusion coefficient of $H^\bullet$ in U. (For interpretation of the references to colour in this figure legend, the reader is referred to the web version of this article.)

timescales for H_2 evolution investigated by Baker et al. A direct, quantitative comparison between their measurements and our calculated percentages of total H_2 outgassed (shown in Fig. 4(b)) is not possible due to differences in the oxidation conditions. However, a qualitative assessment suggests that the relatively long timescales reported in table 3 of Baker et al. (between 15.5 and 600 hours) are likely to be in the region where percentage H_2 asymptotically approaches the theoretical value. A weak time-dependence in the deficiency of evolved H_2 in this regime would therefore be difficult to detect given the level of sample-to-sample variability observed experimentally. As noted by a referee of this work and discussed in [1], the high percentage discrepancy could also be a feature of the Baker et al. experiments being performed close to saturation in an enclosed environment, leading to direct reaction between uranium metal and free H_2. It seems that Baker et al. discounted this mechanism as the main source of hydride formation in their experiments due to i) the absence of any dependence of the quantity of UH_3 formed on the pressure of H_2 allowed to accumulate in the gas phase, and ii) the absence of any significant amount of exchange between hydrogen captured in the UH_3 product and deuterium added to the gas phase (at temperatures below 200 °C) during isotopic studies [3]. These observations, together with the lack of any noticeable pitting on the uranium samples post-exposure, suggest that the bulk hydriding reaction may not have been prevalent in their experiments.

We conclude by revisiting the assumptions of this model. We obviously assume that the reaction scheme specified by (2) holds, but also that any surface processes associated with this reaction can be largely ignored in favour of a static boundary condition for the concentration of OH^-. The model also assumes that the reaction product $H^\bullet$ instantaneously combines to form H_2 at this same surface location. In addition, we also impose a quasi-steady model for the diffusion of OH^- and $H^\bullet$, for which we require relatively low concentrations of OH^-, such that $C^* \ll N_2^*$ (for example). For the spallation of the outer surface we assume that (once established) the adhered layer maintains a constant thickness during the evolution, modelling the cracked layer as a region of substantially higher diffusive transport. Despite these simplifications, the extended RAD model successfully captures many of the key features of uranium oxidation by water vapour at timescales relevant to both the early (parabolic) regime and the later (linear) regime within a consistent theoretical framework that explicitly models the dominant transport and reaction mechanisms. Using this model we have identified the dominant physical parameters, and placed bounds on their values (Fig. 5) for emergent lengthscales of the interfacial hydride to be consistent with current limited observations.

Funding

The work of the first and second authors was supported by AWE plc. The work of the first author was also supported by EPSRC, UK.

CRediT authorship contribution statement

S.R. Monisha Natchiar: Visualization, Validation, Software, Methodology, Investigation, Formal analysis, Writing – original draft. **Richard E. Hewitt:** Visualization, Validation, Supervision, Software, Methodology, Conceptualization, Writing – review & editing. **Phillip D. D. Monks:** Supervision, Data curation, Conceptualization, Writing – review & editing.

Declaration of competing interest

The authors declare that they have no known competing financial interests or personal relationships that could have appeared to influence the work reported in this paper.

Data availability

No data was used for the research described in the article.

References

[1] A. Banos, R. Burrows, T. Scott, A review of the mechanisms, reaction products and parameters affecting uranium corrosion in water, Coord. Chem. Rev. 439 (2021) 213899.
[2] T. Totemeier, Characterization of uranium corrosion products involved in a uranium hydride pyrophoric event, J. Nucl. Mater. 278 (2000) 301–311.
[3] M. Baker, L. Less, S. Orman, Uranium + water reaction. Part 1. Kinetics, products and mechanism, Trans. Faraday Soc. 62 (1966) 2513–2524.
[4] D. Goddard, C. Broan, R. Orr, P. Durham, G. Woodhouse, Uranium hydride studies part III: the kinetics of liquid water and water vapour reactions with uranium hydride, Nat. Nucl. Lab. UK 12545 (2013).
[5] R. Orr, C. Broan, D. Goddard, Uranium hydride studies part IV: summary and conclusions, Nat. Nucl. Lab. UK 12546 (2013).
[6] T. Kondo, F. Beck, M. Fontana, A gas chromatographic study on the kinetics of uranium oxidation in moist environments, Corrosion 30 (1974) 330–341.
[7] C. Colmenares, Oxidation mechanisms and catalytic properties of the actinides, Prog. Solid State Chem. 15 (1984) 257–364.
[8] G.C. Allen, P.M. Tucker, R.A. Lewis, X-ray photoelectron spectroscopy study of the initial oxidation of uranium metal in oxygen+ water-vapour mixtures, J. Chem. Soc. Far. Trans. 2: Mol. Chem. Phys. 80 (1984) 991–1000.
[9] T. Martin, C. Coe, P. Bagot, P. Morrall, G. Smith, T. Scott, M. Moody, Atomic-scale studies of uranium oxidation and corrosion by water vapour, Sci. Rep. 6 (2016) 25618.
[10] S.R.M. Natchiar, R.E. Hewitt, P.D.D. Monks, P. Morrall, Asymptotics of coupled reaction-diffusion fronts with multiple static and diffusing reactants: uranium oxidation in water vapor, SIAM J. Appl. Math. 80 (2020) 2249–2270.
[11] J. Santon, A Kinetic Study of the Reaction of Water Vapor and Carbon Dioxide on Uranium, CEA Grenoble, 1964.
[12] J.M. Haschke, Corrosion of uranium in air and water vapor: consequences for environmental dispersal, J. Alloys Compd. 278 (1998) 149–160.
[13] J.M. Haschke, T.H. Allen, L.A. Morales, Reactions of plutonium dioxide with water and hydrogen–oxygen mixtures: mechanisms for corrosion of uranium and plutonium, J. Alloys Compd. 314 (2001) 78–91.
[14] M. Hedhili, B. Yakshinskiy, T. Madey, Interaction of water vapor with UO_2 (001), Surf. Sci. 445 (2000) 512–525.
[15] A. Ritchie, The kinetics and mechanism of the uranium-water vapour reaction - an evaluation of some published work, J. Nucl. Mater. 120 (1984) 143–153.
[16] K. Winer, C. Colmenares, R. Smith, F. Wooten, Interaction of water vapor with clean and oxygen-covered uranium surfaces, Surf. Sci. 183 (1987) 67–99.
[17] S. Senanayake, H. Idriss, Water reactions over stoichiometric and reduced UO_2 (111) single crystal surfaces, Surf. Sci. 563 (2004) 135–144.
[18] J. Stultz, M. Paffett, S. Joyce, Thermal evolution of hydrogen following water adsorption on defective UO2 (100), J. Phys. Chem. B 108 (2004) 2362–2364.
[19] W. Manner, J. Lloyd, M. Paffett, Reexamination of the fundamental interactions of water with uranium, J. Nucl. Mater. 275 (1999) 37–46.
[20] E. Tiferet, S. Zalkind, M. Mintz, I. Jacob, N. Shamir, Interactions of water vapor with polycrystalline uranium surfaces–the low temperature regime, Surf. Sci. 601 (2007) 936–940.
[21] C.L. Yaws, Thermophysical Properties of Chemicals and Hydrocarbons, William Andrew, 2008.
[22] I. Marchetti, F. Belloni, J. Himbert, P. Carbol, T. Fanghänel, Novel insights in the study of water penetration into polycrystalline UO_2 by secondary ion mass spectrometry, J. Nucl. Mater. 408 (2011) 54–60.
[23] M. Peretz, D. Zamir, G. Cinader, Z. Hadari, NMR study of hydrogen diffusion in uranium hydride, J. Phys. Chem. Solids 37 (1976) 105–111.
[24] M. Mallett, M. Trzeciak, Hydrogen-uranium relationships, Trans. ASM 50 (1958) 16.
[25] V. Wheeler, The diffusion and solubility of hydrogen in uranium dioxide single crystals, J. Nucl. Mater. 40 (1971) 189–194.
[26] R.M. Harker, The influence of oxide thickness on the early stages of the massive uranium–hydrogen reaction, J. Alloys Compd. 426 (2006) 106–117.
[27] A. Banos, T. Scott, A review of the reaction rates of uranium corrosion in water, J. Hazard. Mater. 399 (2020) 122763.